



## Structural and dynamical phase transitions of $\text{NaNbO}_3$ from first-principles calculations

Safari Amisi <sup>1,3</sup>, Philippe Lambin <sup>1,2</sup> and Philippe Ghosez<sup>3</sup><sup>1</sup>Laboratoire de Physique des Solides et des Interfaces,

Institut Supérieur Pédagogique de Bukavu, Democratic Republic of the Congo

<sup>2</sup>Laboratoire de Physique des Solides, Université de Namur, Belgium<sup>3</sup>Physique Théorique des Matériaux, Université de Liège, B-4000 Sart Tilman, Belgium

(Received 12 December 2022; accepted 2 February 2023; published 17 February 2023)

The crystal structures and phase transitions of  $\text{NaNbO}_3$  are analyzed with density functional theory through generalized gradient approximation-PBEsol (GGA-PBEsol) and local density approximations (LDA). The phonon dispersion curves from the high-symmetry cubic perovskite phase are reported to have many unstable branches, predisposing to several combinations of phase transitions to various distorted structures. The coupling between the modes and the strain relaxation play a key role in the condensation of the ground state of sodium niobate. The instabilities at  $R$  and  $M$  points of the first Brillouin zone and along the line  $T$  (connecting the  $M$  and  $R$  points) are very important for stabilizing the low-energy phases. Within the GGA-PBEsol approximation, the ground state is rhombohedral ferroelectric/antiferrodistortive (FE/AFD)  $R3c$ , while in LDA it is rather the orthorhombic FE/AFD  $Pmc2_1$  structure that stabilizes the lowest energy in this compound. In both calculations, there is only a small energy difference between the three lowest-energy phases  $Pmc2_1$  (FE/AFD[110]),  $Pbcm$  (antiferroelectric/AFD), and  $R3c$  (FE/AFD[111]), which is a key characteristic of antiferroelectricity. The GGA-PBEsol approach provides more sensible results than the LDA approximation.

DOI: [10.1103/PhysRevMaterials.7.024408](https://doi.org/10.1103/PhysRevMaterials.7.024408)

### I. INTRODUCTION

Antiferroelectric (AFE) materials are promising candidates for a wide range of electronic applications, such as, high-energy storage capacitors [1], electrocaloric refrigerators [2], and nonvolatile random access memories [3]. Among them,  $\text{NaNbO}_3$  (NNO), known for its complex structures and phase transitions [4,5], is one of the very few lead-free antiferroelectric oxides. This material has attracted considerable interest because it is a typical nontoxic and highly stable semiconductor which has applications in photocatalysis [6] and potentially also in piezoelectric nanodevices [7]. Indeed, NNO has shown growing interest in environmental protection, providing a matrix phase for various lead-free piezoelectric materials, such as  $(\text{K}, \text{Na}, \text{Li})(\text{Nb}, \text{Ta}, \text{Sb})\text{O}_3$  [8] and  $(\text{Na}, \text{K})\text{NbO}_3$  [9], which could replace the set of lead-based perovskites.

$\text{ABO}_3$  perovskites typically crystallize at high temperature in an aristotype cubic  $Pm\bar{3}m$  structure, but then lower their symmetry on cooling by rotating or distorting the  $\text{BO}_6$  octahedra and translating the  $A$  site or  $B$  site cations. The structures obtained by simple rotations of the  $\text{BO}_6$  octahedra around the axes of the aristotype cubic structure were first classified by Glazer [10], followed by a number of theoretical studies of the possible tilt structures and phase transitions [11–13]. It is known today that understanding the crystal structures, characterized by structural phase transitions, of the perovskites is crucial to understanding the origin of their performance and accelerate the search for new materials. The computational

first-principles approach has become an extremely valuable tool to identify competing structural instabilities in perovskites and this is even more crucial for a structurally complex material such as NNO.

The richness of the phonon curves in the cubic phase and the complex sequence of phase transitions of NNO are the subject of several studies both experimental and theoretical. Discovered in 1949 by Matthias [14], NNO certainly represents the most structurally complex “simple” perovskite known so far. A set of “seven phases of sodium niobate” were first summarized by Megaw [15] (PE, AFD, AFE, and FE are abbreviations for paraelectric, antiferrodistortive, antiferroelectric, and ferroelectric, respectively):  $N$  (FE/AFD- $R3c$ , below  $-100^\circ\text{C}$ ),  $P$  (AFE/AFD- $Pbcm$ , from  $-100$  to  $360^\circ\text{C}$ , room temperature),  $R$  (AFE/AFD- $Pnmm$ ,  $360 \rightarrow 480^\circ\text{C}$ ),  $S$  (PE/AFD- $Pnmm$ ,  $480 \rightarrow 520^\circ\text{C}$ ),  $T_1$  (PE/AFD- $Cmcm$ ,  $520 \rightarrow 575^\circ\text{C}$ ),  $T_2$  (PE/AFD- $P4/mbm$ , de  $575 \rightarrow 640^\circ\text{C}$ ), and  $U$  (PE- $Pm\bar{3}m$ , beyond  $640^\circ\text{C}$ ). Since then, several additional phases have been put forward. It is the case of the  $Q$  (FE/AFD- $Pmc2_1$ ) phase, visible as a phase coexisting in certain temperature ranges with the  $N$  and  $P$  phases [16–20].

In spite of the importance of phonons in the physics of ferroelectrics, there are rare studies in the literature on the phonon-dispersion relation of NNO from first principles [21]. The present study is part of the first-principles contributions to improve our understanding of the crystal structures, phase transitions, and phase stability of sodium niobate.

In this paper we quantify the delicate competitions between instabilities in NNO, we systematically analyze the phase

transition mechanism and discuss how it affects the volume and atomic displacements. We confirm the presence of mixtures of the  $Pmc2_1$  (FE[110]/AFD),  $Pbcm$  (AFE/AFD), and  $R3c$  (FE[111]/AFD) polymorphs. Compared to experimental observations, our generalized gradient approximation–PBEsol (GGA-PBEsol) approach provides more sensible results than local density approximations (LDA). However, let us notice the fact that the  $R$  AFE/AFD- $Pnmm$  and  $S$  PE/AFD- $Pnmm$ , with cells dimension  $\sqrt{2} \times \sqrt{2} \times 12$  (24 formula units) and  $\sqrt{2} \times 6 \times \sqrt{2}$  (12 formula units), respectively, are more complex to build and to characterize from *ab initio* simulations [22].

The remainder of this paper is organized as follows. In the Sec. II, we summarize the technical details of our calculations. Then the description of the cubic perovskite phase, including the lattice constant, the Born effective charges, and the phonon dispersion curves are reported in Sec. III. Section IV discusses the FE, AFD, and antipolar electric (APE) instabilities condensed one by one and the relative low-energy structure for each them. In Sec. V, we investigate the ground state in NNO and the energy proximity between FE and AFE phases. We provide a summary at the end.

## II. COMPUTATIONAL DETAILS

First-principles calculations were carried out using the ABINIT density functional theory (DFT) package [23–25] within the plane-wave-pseudopotential approach. We used the Perdew-Burke-Ernzerhof functional revised for solids (GGA-PBEsol) [26] and optimized norm-conserving pseudopotentials (ONCVSP) [27–29], available on the PSEUDO-DOJO server [30]. For comparison, some results have also been checked at the LDA level [31]. The valence states for the computations are  $2s^2 2p^6 3s^1$  for Na,  $4s^2 4p^6 4d^4 5s^1$  for Nb and  $2s^2 2p^4$  for O. Convergence was achieved for an energy cutoff of 45 hartrees for the plane-wave expansion (for both types of pseudopotentials) and a  $8 \times 8 \times 8$  grid of  $k$ -points for the Brillouin zone sampling of the single perovskite five-atom cell. In supercell calculations, the  $k$ -points' grid was adjusted to provide a density of  $k$ -points and a degree of convergence similar to the  $8 \times 8 \times 8$  sampling in the five-atom cell. When condensing the AFD instabilities, either we considered a 20-atom supercell corresponding to  $\sqrt{2}a_0, \sqrt{2}a_0, 2a_0$ , with a sampling of  $6 \times 6 \times 4$   $k$ -points or, for the  $Cmcm, Pmmn, R\bar{3}c$ , and  $R3c$  phases, a 40-atom supercell corresponding to  $2a_0, 2a_0, 2a_0$  with a sampling of  $4 \times 4 \times 4$   $k$ -points. The antipolar electric (APE)  $Cmc2_1$ , AFD  $a^- a^- b^+ / a^- a^- b^-$ , and AFE/AFD  $Pbcm$  structures were relaxed in a 40 atoms supercell corresponding to  $\sqrt{2}a_0, \sqrt{2}a_0, 4a_0$ , and a sampling of  $6 \times 6 \times 2$   $k$ -points. We explicitly checked that the relative energy of the different phases is well converged and independent of the choice of the supercell. All of the present *ab initio* calculations were performed using optimized theoretical lattice constants. Full structural relaxations (lattice parameters and internal degrees of freedom) were performed until the forces and stresses were smaller than  $10^{-7}$  hartrees/bohr and  $10^{-7}$  hartrees/bohr<sup>3</sup>, respectively. The phonon frequencies, Born effective charges, and electronic dielectric tensor were calculated according to density functional perturbation theory (DFPT) [32]. The phonon dispersion curves were interpolated

from the dynamical matrices on a  $2 \times 2 \times 2$   $q$ -point grid, while treating separately the dipole-dipole interaction. For the polarization, we used the Berry phase approach [33]. The space group symmetry were checked by the FINDSYM program [34]. To analyze the group theory and relative contributions of different phonon modes to the distortions we employed ISOTROPY and AMPLIMODES codes of the Crystallographic Bilbao server [35–37].

## III. HIGH-SYMMETRY CUBIC STRUCTURE

First, we report the properties of the highly symmetric cubic perovskite structure of NNO. In this cubic phase, the atomic positions are fixed by symmetry and the only structural parameter to be relaxed is the lattice constant  $a_0$ . Our results are reported in Table I compared to NaTaO<sub>3</sub> (AFD), KNbO<sub>3</sub> (FE), and KTaO<sub>3</sub> (PE), and other theoretical and experimental values. We report also the Born effective charges ( $Z^*$ ) and the optical dielectric constant ( $\epsilon^\infty$ ). In the cubic structure,  $Z^*$  of  $A$  ( $A = \text{Na}; \text{K}$ ) and  $B$  ( $B = \text{Nb}; \text{Ta}$ ) atoms are isotropic while, for O, two distinct values have to be considered depending if the O atom is displaced along the  $B$ -O chain ( $O_{\parallel}$ ) or perpendicularly to it ( $O_{\perp}$ ).

Our NNO relaxed lattice constant ( $a_0 = 3.9427\text{\AA}$ ) is in agreement with that reported experimentally ( $a_0 = 3.945\text{\AA}$ ) and other theoretical results (Table I). Let us nevertheless point out the discrepancy with the values found by Prosandeev [39] who used the ultrasoft atomic potentials (US-PP).

The Born effective charges of  $B$  ( $B = \text{Nb}; \text{Ta}$ ) and  $O_{\parallel}$  are strongly anomalous and these values are known to be a common feature of  $ABO_3$  compounds. They are related to the dynamical transfer of charge between the  $B$   $d$  and  $O$   $2p$  orbitals [42].  $Z^*_{(\text{Na/K})}$  and  $Z^*_{O_{\perp}}$  are also anomalous but to a much lower extent. We notice the tendency of the Born effective charges to be larger in niobates (ANbO<sub>3</sub>) than in tantalates (ATaO<sub>3</sub>). In the same way, the calculated optical dielectric constant of ANbO<sub>3</sub> (6.12 and 6.42) is bigger than for ATaO<sub>3</sub> (5.12 and 5.39).

Our calculations describe NNO as an insulator with an indirect band gap of 1.65 eV between  $R$  and  $\Gamma$  points, as well as for NaTaO<sub>3</sub> (2.32 eV), KNbO<sub>3</sub> (1.53 eV), and KTaO<sub>3</sub> (2.16 eV). This result is in agreement with the previous theoretical value 1.6 eV [40]. Compared with the experimental band gap 3.4 eV of NNO [43], the calculated indirect band gap is much smaller. This discrepancy is due to the use of GGA, or LDA, which typically underestimates, by about 30 to 40%, the experimental band gap in semiconductors and insulators [44] but correctly reproduces their insulating nature. Note, however, that hybrid functionals give a band-gap value in much better agreement with the experiment, as demonstrated by distinct authors [45–47], while the Hartree-Fock (HF) method very strongly overestimates the *ab initio* calculated band gaps of solids [47].

Even if the ground state of a system can be very complex, the calculation of phonon dispersion curves in the high-symmetry phase offers a global view of the instabilities that can progressively condense and helps revealing the possible intermediate phases and the ground state. The Goldschmidt tolerance factors of NNO ( $t < 0.98$ ) and NaTaO<sub>3</sub> (NTA) materials are close and dispose them to stabilize an orthorhombic

TABLE I. Lattice parameter ( $\text{\AA}$ ), Born effective charges ( $|e|$ ), optical dielectric constant gap (eV), and the calculated Goldschmidt tolerance factor  $t$  of cubic  $\text{NaNbO}_3$  at relaxed volume compared to  $\text{NaTaO}_3$  (AFD),  $\text{KNbO}_3$  (FE), and  $\text{KTaO}_3$  (PE), and other theoretical values. The nominal charge are  $+1|e|$  for Na and K ions,  $+5|e|$  for Nb and Ta ions, and  $-2|e|$  for O ion. The  $\text{NaNbO}_3$  experimental lattice parameter and gap are, respectively,  $3.945 \text{ \AA}$  and  $3.4 \text{ eV}$  [38].

	$\text{NaNbO}_3$			$\text{NaTaO}_3$ Present	$\text{KNbO}_3$ Present	$\text{KTaO}_3$ Present
	Present	LDA	US-PP [39]			
$a_0$	3.9427 <sup>a</sup> 3.9134 <sup>b</sup>	3.92 [40]	4.1822	3.9366 <sup>a</sup>	3.9847 <sup>a</sup>	3.9772 <sup>a</sup>
$Z_A^*$	1.13	1.13 [41]	1.102	1.14	1.14	1.15
$Z_B^*$	9.48	9.11	9.718	8.56	9.61	8.68
$Z_{O_{\parallel}}^*$	-7.28	-7.01	-6.28	-6.50	-7.28	-6.49
$Z_{O_{\perp}}^*$	-1.67	-1.61	-2.27	-1.60	-1.73	-1.67
$\epsilon^{\infty}$	6.12	4.96		5.12	6.42	5.39
GAP	1.65	1.6 [40]		2.32	1.53	2.16
$t$	0.94			0.92	1.04	1.02

<sup>a</sup>GGA-PBEsol.

<sup>b</sup>LDA.

AFD phase. In Fig. 1 we report the phonon dispersion curves of NNO and NTA in a cubic five-atom cell. The  $R$ - $\Gamma$ ,  $\Gamma$ - $X$ ,  $X$ - $M$ , and  $M$ - $\Gamma$  lines are along the  $[111]$ ,  $[100]$ ,  $[010]$ , and  $[110]$  directions, respectively. Negative values of  $\omega$  ( $\text{cm}^{-1}$ ) in

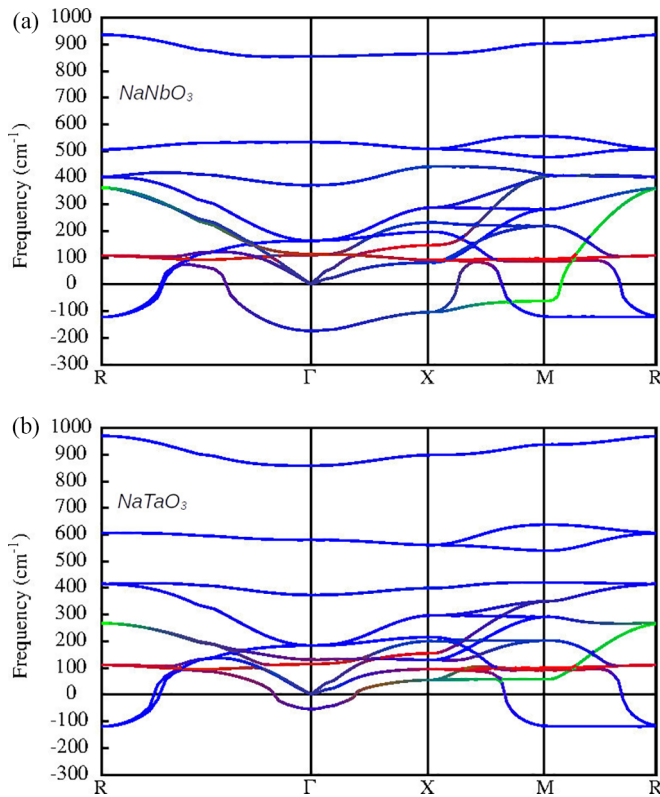


FIG. 1. Calculated phonon dispersion curves of cubic (a)  $\text{NaNbO}_3$  and (b)  $\text{NaTaO}_3$  at the GGA-PBEsol relaxed volume along the path  $R$ - $\Gamma$ - $X$ - $M$ - $R$  of the cubic Brillouin zone. A color is assigned to each point based on the contribution of each kind of atom to the associated dynamical matrix eigenvector (red for the Na atom, green for the Nb/Ta atom, and blue for O atoms). The  $\Delta$  and  $T$  points of the Brillouin zone in NNO are not represented here.

the graphs correspond to imaginary phonon frequencies and are related to unstable modes, which determine the nature of eventual phase transitions. By condensing these unstable modes, it is theoretically possible to find the intermediate and the stable phases of a compound. The character of these modes thus also has significant implications on system properties. Frequencies and types of ferroic unstable modes are summarized in Table II.

Our cubic NNO phonon curves are in agreement with those calculated by Machado *et al.* [21] but different from those calculated by Prosandeev [39], in which the  $R$  unstable mode is the most significant. As can be seen from Fig. 1, the ferroelectric instability in NNO, contrary to that in NTA, is not restricted to the  $\Gamma$  point, but extends to the  $\Gamma$ - $X$ - $M$  plane and the AFD unstable branches extend from  $M$  to  $R$  in both structures. In NNO there are additional unstable branches.

In NTA, instabilities are dominated by AFD  $R_4^+$  and  $M_3^+$  modes, but in NNO, similar to what is observed for  $\text{PbZrO}_3$  (PZO) [48], the polar FE ( $\Gamma_4^-$ ) and antipolar ( $\Delta_5$ ,  $X_5^-$ ,  $M_3^-$  and  $T_4$ ) instabilities are also significant. For the instability at the  $\Gamma$  point, the eigendisplacement in NTA is significantly

TABLE II. Modes and soft phonon frequencies  $\omega$  ( $\text{cm}^{-1}$ ) of NNO and NTA high symmetry at  $\Gamma$ ,  $X$ ,  $M$ ,  $R$ ,  $\Delta$ , and  $T$  points of the Brillouin zone. AP is the abbreviation of antipolar mode. The values in brackets are from Prosandeev [39].

$k$ -points	Mode	Type	$\omega$		
			$\text{NaNbO}_3$	$\text{NaTaO}_3$	
$\Gamma$	$(0, 0, 0)$	$\Gamma_4^-$	FE	174i (121i)	54i
$\Delta$	$(0, \frac{1}{4}, 0)$	$\Delta_5$	AP	129i	
$X$	$(\frac{1}{2}, 0, 0)$	$X_5^-$	AP	103i	
$M$	$(\frac{1}{2}, \frac{1}{2}, 0)$	$M_3^+$	AFD	120i (138i)	118i
		$M_3^-$	AP	62i	
$T$	$(\frac{1}{2}, \frac{1}{2}, \frac{1}{4})$	$T_4$	AFD/AP	121i	
$R$	$(\frac{1}{2}, \frac{1}{2}, \frac{1}{2})$	$R_4^+$	AFD	122i (140i)	120i

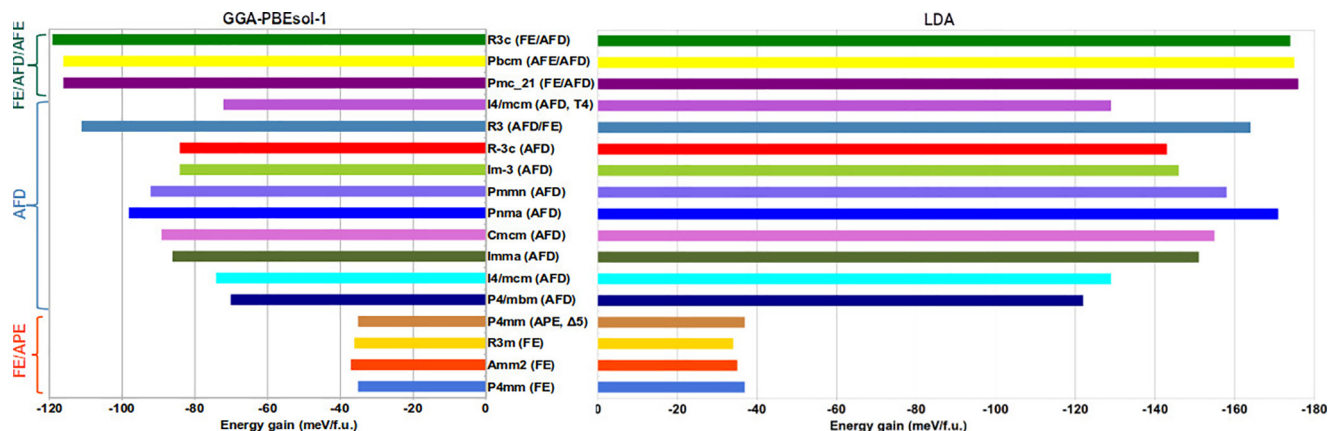


FIG. 2. Energy gain (meV/f.u.) of different total relaxed structures in NNO calculated in two approximation GGA-PBEsol and LDA. Magnitudes of the GGA-PBEsol tilt angles ( $^{\circ}$ ) are :  $P4/mbm$  ( $a^0a^0c^+$ :  $c^+ = 11.3/5.0^{\circ}$ ),  $I4/mcm$  ( $a^0a^0c^-$ :  $c^- = 11.9$ ),  $Imma$  ( $a^-a^-c^0$ :  $a^- = 9.0$ ),  $Cmcm$  ( $a^0b^-c^+$ :  $b^- = 8.7/4.7$  [49],  $c^+ = 9.0/6.1$ ),  $Im\bar{3}$  ( $a^+a^+a^+$ :  $a^+ = 7.0$ ),  $R\bar{3}c$  ( $a^-a^-a^-$ :  $a^- = 6.9$ ),  $Pnmm$  ( $a^-b^+b^+$ :  $a^- = 8.0$ ,  $b^+ = 6.9$ ),  $Pnma$  ( $a^-b^+a^-$ :  $a^- = 8.5$ ,  $b^+ = 9.4$ ). The zero of energy corresponds to the equilibrium cubic paraelectric  $Pm\bar{3}m$  state.

dominated by the movement in opposite directions of Na and O atoms, with a very small displacement of the Ta atom, surely because of its heaviness (almost six times the mass of Na). In NNO, with Nb being lighter than Ta and of close ionic radius, all atoms contribute significantly to the eigendisplacements of the polar instability. The condensation of unstable modes is different depending on whether the transition atom is Ta or Nb in  $NaBO_3$  ( $B = Ta, Nb$ ). For NTA, the condensation of the AFD modes stabilizes in the  $Pnma$  ground state all the other unstable modes observed in the high-symmetry phase. In NNO, however, as we shall see in Sec. V, it is rather the combined condensation of all these modes, at least two as in the  $R\bar{3}c$  structure that stabilizes the low-energy structures. Let us first analyze the NNO phonons unstable modes separately.

#### IV. INDIVIDUAL STRUCTURAL INSTABILITIES

In this section, we successively analyze the condensations of different unstable modes observed in the phonon curves of the high-symmetry phase. The goal is to see how these modes condense when isolated and when combined and thus to understand the importance of the couplings in the stabilization of this or that phase. The colored bars of Figs. 2 and 3 show the energy gains relative to the high-symmetry cubic phase of different structures that we relaxed in NNO according to two approximations (GGA-PBEsol and LDA). In the GGA-PBEsol approximation, we performed two types of calculations: the GGA-PBEsol-1 (Fig. 2, left) calculation consisted in a total relaxation of the cell parameters and atomic positions while the GGA-PBEsol-2 (Fig. 3) calculation consisted in relaxing only the atomic positions but in a fixed cubic cell, i.e., not allowing for strain.

Three zones can be identified in these graphs: the first one with small energy gains associated to the condensation of polar (FE) and antipolar electric (APE) instabilities, the second with much larger energy gains associated to the condensation of AFD instabilities, and the third one with the largest energy gains associated to the condensation of combined FE/AFD and AFD/APE instabilities. The condensation

of either FE/APE and AFD instabilities will be discussed here while their combination will be considered in the Sec. V.

#### A. Polar and antipolar instabilities

Looking at the phonon dispersion curves of the cubic phase (Fig. 1), the unstable polar mode is the most significant ( $\Gamma_4^-, 174i \text{ cm}^{-1}$ ) followed by the antipolar electric mode ( $\Delta_5, 129i \text{ cm}^{-1}$ ). In agreement with the previous study [21], our analysis of the eigendisplacements corresponding to the  $\Gamma_4^-$  phonons shows that the B-Nb atoms are indeed involved in the motion in such a way that both atoms Na and Nb move out of phase with respect to the oxygen atoms (Table III), in contrast to what it is observed in the PZO polar unstable mode; so the Nb atom contributes significantly to the ferroelectric  $\Gamma_4^-$  mode in NNO. The mode-effective charge associated to this unstable mode is  $7.88e$ , larger than in NTA and PZO.

The  $P4mm$  (royal blue bars, Fig. 2),  $Amm2$  (orange-red bars), and  $R3m$  (gold bars) structure represent the condensations of the unstable polar modes along the directions [100], [110], and [111], respectively. The energy difference between

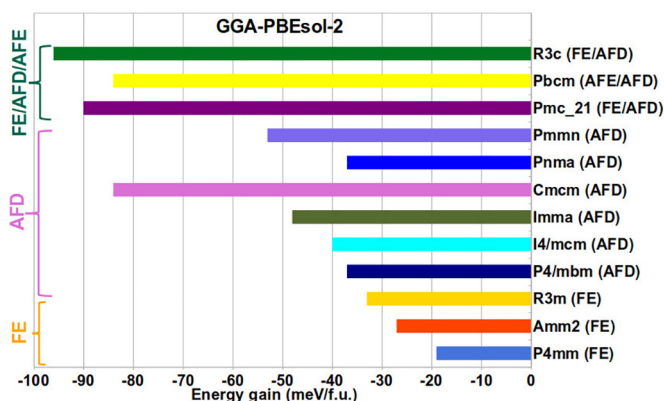


FIG. 3. Energy gain (meV/f.u.) of different structures of NNO calculated by relaxing only the atomic positions but in a cubic volume, i.e., by not allowing the strain (GGA-PBEsol-2).



TABLE III. Normalized real-space eigendisplacement for the unstable FE mode at  $\Gamma$  ( $z$  polarization) and associated TO mode effective charges (as defined in Ref. [32]). The corresponding dynamical matrix eigenvector can be obtained by multiplying each value by the appropriate mass factor  $\sqrt{M_{\text{ion}}}$ .

Atom	NaNbO <sub>3</sub>	NaTaO <sub>3</sub>	PbZrO <sub>3</sub>
Na	0.046	0.112	0.034
Nb/Ta/Zr	0.051	0.016	-0.014
$O_{\parallel}$	-0.107	-0.087	-0.067
$O_{\perp}$	-0.128	-0.130	-0.145
$\bar{Z}^*$	7.88	5.36	5.07

the three structures is very small, about 1 meV/f.u. If NNO were only FE, according to the approximation used, the  $Amm2$  structure would be the most stable FE GGA-PBEsol structure in this material ( $Amm2$ : -37 meV/f.u.;  $R3m$ : -36 meV/f.u.; and  $P4mm$ : -35 meV/f.u.) with a spontaneous polarization equal to 49  $\mu\text{C}/\text{cm}^2$  and an indirect  $R$ - $\Gamma$  gap of 2.1 eV. Our LDA calculations gives a different trend; it is rather the  $P4mm$  structure which is the FE lowest energy ( $P4mm$ : -37 meV/f.u.;  $Amm2$ : -35 meV/f.u.; and  $R3m$ : -34 meV/f.u.). Contrary to the intuition that one would have by observing the intensities of the instabilities in the phonon curves (Fig. 1), the condensation of the only FE unstable mode allows small energy gains. Concerning the APE unstable mode  $\Delta_5$ , starting from the  $Cmc2_1$  structure the system relaxes in the  $P4mm$  structure ( $\Gamma_4^-$ , peru bars) with the almost same total energy gain in both GGA-PBEsol and LDA (-35/ -37 meV/f.u.). This result allows us to conclude that, unlike the  $\Sigma_2$  APE mode in PZO [48], the  $\Delta_5$  APE mode in NNO cannot even condense itself.

### B. Antiferrodistortive instabilities

Among all instabilities, those caused by the rotations of oxygens octahedra, antiferrodistortive (AFD) modes, are the most common in perovskites [10–13]. Glazer's description are in terms of component tilts around the "pseudocubic" axes, that is, the cubic axes of the parent structure. The irreducible representation (irrep) associated with the in-phase tilts is  $M_3^+$  ( $k = 1/2, 1/2, 0$ ) and that associated with the antiphase tilts is  $R_4^+$  ( $k = 1/2, 1/2, 1/2$ ) [13]. Both AFD modes are unstable in the high-symmetry cubic phase of NNO with significant intensities ( $M_3^+$ :  $120i$  and  $R_4^+$ :  $122i$ ), but, contrary to what was observed in PZO [48], not higher but lower than polar FE and antipolar modes ( $\Gamma_4^-$ ,  $174i \text{ cm}^{-1}$  and  $\Delta_5$ ,  $129i \text{ cm}^{-1}$ , respectively).

Now let us see how NNO would behave if it were only AFD. In the second zone of the Fig. 2 (AFD distortion), we show the total relaxed energies of the AFD structures obtained by condensing the  $M_3^+$  and  $R_4^+$  modes, separated and combined. Whatever the approximation used, the hierarchy of AFD unstable modes stay the same. The lowest energy is achieved in the orthorhombic phase  $Pnma$  ( $a^-b^+a^-$ ), combining two antiphase and one in-phase rotations, as also found in PZO [48]. This phase is not observed in NNO, but it may allow us to understand why the coupling of its rotations with the polar FE orthorhombic displacements favors

a significant energy gain to stabilize the  $Pmc2_1$ , a subgroup of  $Pnma$ . The AFD  $P4/mbm$  ( $a = b = 5.4756/5.5639$  [49],  $c = 7.9066/7.8856$ ) and  $Cmcm$  ( $a = 7.7195/7.7642$  [49],  $b = 7.8061/7.8550$ ,  $c = 7.8109/7.8696$ ) phases were observed experimentally. On the one hand, from the results of our calculations, both AFD modes inphase  $M_3^+$  and antiphase  $R_4^+$  evolve almost in the same way when they are separately condensed in one, two, or even three components. The structures  $Im\bar{3}$  ( $a^+a^+a^+$ , yellow-green bars) and  $R\bar{3}c$  ( $a^-a^-a^-$ , red bars), condensing, respectively, the  $M_3^+$  and  $R_4^+$  modes in three components show the same energy gain (-84 meV/f.u., even if the LDA approximation slightly favors the  $Im\bar{3}$  structure, -146 meV/f.u., more than the  $R\bar{3}c$ , -143 meV/f.u.), but their couplings with polar displacements favor the  $R_4^+$  mode ( $R3c$ ,  $a_p^-a_p^-a_p^-$ , -119/ -174 meV/f.u., green bars) more than the  $M_3^+$  mode ( $R3$ ,  $a_p^+a_p^+a_p^+$ , -111/ -164 meV/f.u., steel blue bars). On the other hand, we can notice that condensing  $M_3^+$  and  $R_4^+$  modes simultaneously ( $Cmcm$ ,  $a^0b^-c^+$ , -89/ -155 meV/f.u., orchid bars) is more favorable than condensing a single mode in two ( $Imma$ ,  $a^-a^-c^0$ : -86/ -151 meV/f.u., dark olive-green bars) or three ( $Im\bar{3}$  or  $R\bar{3}c$ ) directions. Moreover, coupling antiphase tilts in two directions and in-phase tilt in the third direction ( $Pnma$ ,  $a^-b^+a^-$ : -98/ -171 meV/f.u., blue bars) is energetically more favorable than combining antiphase tilt in one direction and in-phase tilts in two directions ( $Pnmm$ ,  $a^-b^+b^+$ : -92/ -158 meV/f.u., medium slate-blue bars).

Compared to the energy gain of the FE mode  $\Gamma_4^-$  (-37 meV/f.u.), we can see that the energy gains of the AFD modes  $M_3^+$  and  $R_4^+$ , both separately and combined, are considerably larger (from 1.9 to 2.6 times for  $P4/mbm$  and  $Pnma$ , respectively). This can explain why octahedral tilts corresponding to the  $M_3^+$  and  $R_4^+$  modes can be considered as primary order parameters, inducing the first two structural transitions, from the cubic into the  $T_2$  and  $T_1$  phases [21]. The AFD modes therefore play a crucial role in condensing the NNO ground state, as they select the AFE distortions, among competing structural variants, and at low temperature the rhombohedral  $R3c$  and the orthorhombic  $Pmc2_1$  (both FE/AFD) symmetries which are energetically close to the orthorhombic AFE/AFD state  $Pbcm$ .

The significantly different gain of energy arising from AFD and APE distortions is at odds with that observed in PZO [48], another AFE compound. While in PZO, the condensation of the  $\Sigma$  APE and  $S_4$  AFD distortions converges to energies close to those obtained in  $Imma$  and  $Pnma$  structures (-215, -214, -169, and -224 meV/f.u., respectively), the situation is different in NNO. Indeed, the condensation of the individual  $\Delta_5$  and  $T_4$  distortions converges at total energies far higher than the  $Imma$ ,  $Cmcm$ , and  $Pnma$  structures (-16, -72, -86, -89, and -98 meV/f.u., respectively). The coupling of modes is very crucial in this material to stabilize the low-energy states FE/AFD and AFE/AFD and, as we have seen before, it is the unstable AFD modes that allow to lower the energies of the FE and APE modes.

### C. Phonon-strain coupling

Comparing the energy gains of GGA-PBEsol-1 and GGA-PBEsol-2 calculations, we notice that the strain relaxation

TABLE IV. Energy gain (meV/f.u.), remanent instability ( $\text{cm}^{-1}$ ), and total polarization  $P$  ( $\mu\text{C}/\text{cm}^2$ , Exp.  $59 \mu\text{C}/\text{cm}^2$  in  $R3c$  [50]) of the three low-energy distortions in NNO optimized through GGA-PBEsol (GGAPBEs) and LDA approximations. The comparative values in brackets are taken from Ref. [51]. The angle in the rhombohedral cell is  $89.24^\circ$  (Exp.  $89.22^\circ$  [52]). The condensed modes in the  $30i$  instability are relatively  $R_4^+$  (1.45),  $T_4$  (1.20), and  $\Delta_5$  (0.65).

Space group	Energy gain		Instability		$P$
	GGAPBEs	LDA	GGAPBEs	LDA	
$Q: Pmc2_1$	-116.1(-108.7)	-176.2	$0i$	$0i$	32(47)
$P: Pbcm$	-116.3(-106.3)	-175.0	$30i$	$0i$	
$N: R3c$	-119.2(-116.1)	-173.9	$0i$	$0i$	48(58)

plays a significant role in NNO, lowering the energy by 3 meV/f.u. in  $R3m$  and by 61 meV/f.u. in  $Pnma$ . It is the strain relaxation that allows to stabilize the  $Amm2$  structure (from  $-27$  to  $-37$  meV/f.u.) below the  $R3m$  (from  $-33$  to  $-36$ ) and also the  $Pnma$  (from  $-37$  to  $-98$  meV/f.u.) below the  $Cmcm$  (from  $-50$  to  $-89$  meV/f.u.) and the  $Pmnm$  (from  $-53$  to  $-92$  meV/f.u.). It is also the strain relaxation that brings  $Pbcm$  and  $Pmc2_1$  structures at similar energies (from  $-86$  to  $-116$  meV/f.u. and from  $-90$  to  $-116$  meV/f.u., respectively). As for the  $R3c$  symmetry, it remains the most stable (from  $-96$  to  $-119$  meV/f.u.).

## V. TOWARDS THE ENERGY GROUND STATE

Having explored the modes separately, we are now in a position to investigate the combinations of modes yielding the lowest-energy structures. As can be seen from Figs. 2, and whatever the approximation used, three structures show comparable low-energy values: (i) The rhombohedral FE/AFD[111]  $R3c$  phase (green bars), also called the  $N$  phase, which is the experimental ground state; (ii) the orthorhombic AFE/AFD  $Pbcm$  phase (yellow bars), also called the  $P$  phase, which is the room-temperature antiferroelectric phase and (iii) the orthorhombic FE/AFD[110]  $Pmc2_1$  (mauve bars), also called the  $Q$  phase, which has been proposed [16,17] as the ferroelectric phase induced by applying an electric field to the  $Pbcm$  phase at room temperature. The energy lowering (respect to the high-symmetry cubic reference  $Pm\bar{3}m$ ) of these three phases as obtained from GGA-PBEsol and LDA approximations, are reported in Table IV.

The coexistence of polar and nonpolar phases, arising from distinct small distortions of the same reference structures and showing very similar low energies was discussed by Rabe [53] as a key requirement for antiferroelectricity and was also observed in  $\text{PbZrO}_3$  [48]. Depending on the approximation used, our calculations lead to two distinct results regarding the energy ordering of those phases.

When we consider the GGA-PBEsol approximation, it is the  $R3c$  structure which constitutes the NNO lowest-energy state, in agreement with previous experimental and theoretical [21,51] studies. This is also in agreement with previous generalized gradient approximation using the functional proposed by Wu and Cohen (GGA-WC) calculation, although stabilizing further the  $R3c$  phase.

In GGA-PBEsol, even keeping the cubic volume fixed (Fig. 3), i.e., not relaxing the strain, the low-energy structure remains  $R3c$  ( $-96$  meV/f.u.) followed by  $Pmc2_1$  ( $-90$  meV/f.u.) and  $Pbcm$  ( $-84$  meV/f.u.). We can notice again here the importance of the strain in all these structures, making them gaining about 20 meV/f.u., much more in the  $Pbcm$  (relative energy gain of 32 meV/f.u.) which stabilizes it at the same energy state as the  $Pmc2_1$ . In our calculations we get  $E(N) < E(P) \approx E(Q)$  while in Ref. [51] they reported  $E(N) < E(Q) < E(P)$ , but we notice that the energy differences remain small.

When we consider the LDA approximation, the situation changes: it is now the  $Pmc2_1$  structure that is the lowest-energy structure followed by  $Pbcm$  and then  $R3c$ . Even using the LDA with alternative Troullier-Martins pseudopotentials (LDA-TM), we get the same sequence. These results allows us to conclude that the LDA is not a suitable functional to study NNO in the sense that it does not stabilize the appropriate ground state and the GGA-PBEsol should be preferred.

The polar  $R3c$  ( $a_+^- a_+^- a_+^-$ ,  $a^- = 7.1^\circ$ ) phase combines the antiphase tilts ( $R_4^+$  mode,  $a^- a^- a^-$  pattern) and polar displacements ( $\Gamma_4^-$  mode) of the Na, Nb, and O atoms along three cubic directions [111]. As for the  $Pbcm$  phase, it combines the  $Imma$  ( $R_4^+$  mode,  $a^- a^- c^0$  pattern) distortion with  $T_4$  (complex AFD) and  $\Delta_5$  (APE). Finally, the  $Pmc2_1$  phase, defined as a subgroup of the  $Pnma$  phase, shows an unusual distortion; condensing complex rotations on alternative layers  $a^- a^- b^+ / a^- a^- b^-$  ( $a^- = 6.8^\circ$ ,  $b^+ = 8.3^\circ$  and  $b^- = 6.9^\circ$ ) as in  $Pbcm$ , but while the  $Pbcm$  phase favors APE motion in the orthorhombic  $ab$ -plane, i.e., in the cubic direction [100], the  $Pmc2_1$  phase is polar along the orthorhombic  $b$ -axis, i.e., in the cubic plane [110]. The structural similarities between the last two phases and their close energies allows us to support that, at room temperature, the AFE- $Pbcm$  phase of NNO should transform into the FE- $Pmc2_1$  phase on the application of electric field [16,17].

The low energy of the  $Pmc2_1$  structure results mainly from the high stability of the  $Pnma$  phase. The calculated spontaneous polarization of NNO for the FE/AFD  $Pmc2_1$  and  $R3c$  structures given in Table IV are found to be  $32 \mu\text{C}/\text{cm}^2$  and  $48 \mu\text{C}/\text{cm}^2$ , respectively, which is comparable to that we obtained for the conventional ferroelectric rhombohedral  $\text{KNbO}_3$  ( $41 \mu\text{C}/\text{cm}^2$ ) and  $\text{BaTiO}_3$  ( $42 \mu\text{C}/\text{cm}^2$ ), but significantly smaller than tetragonal  $\text{PbTiO}_3$  ( $97 \mu\text{C}/\text{cm}^2$ ).

Concerning the  $Pmc2_1$  structure, we relaxed also two other subgroups of the  $Pnma$  phase, namely,  $Pna2_1$  and  $Pnm2_1$  [20]. The last two structures converge to a similar total energy which remains higher than the total relaxed energy of the  $Pmc2_1$  (GGA-PBEsol:  $-111/-116$  and LDA:  $Pnm2_1 = -174/Pna2_1 = -175/-176$  meV/f.u., respectively). This result allows us to state that, of the three subgroups of the  $Pnma$  distortion, the  $Pna2_1$  and  $Pnm2_1$  distortions are unlikely in NNO in favor of the more stable  $Pmc2_1$  structure. Concerning the  $30i$  instability observed in the  $Pbcm$  phase, its condensation gives the  $Pca2_1$  structure. When we condense this last structure, according to what was found in Ref. [22], its total energy is not significantly lower than  $Pbcm$  using either LDA ( $-175.0$  meV/f.u.) or GGA-PBEsol ( $-116.4/-116.3$  meV/f.u.  $\Rightarrow -0.1$  meV/f.u.) calculation. This means that the  $P$  phase

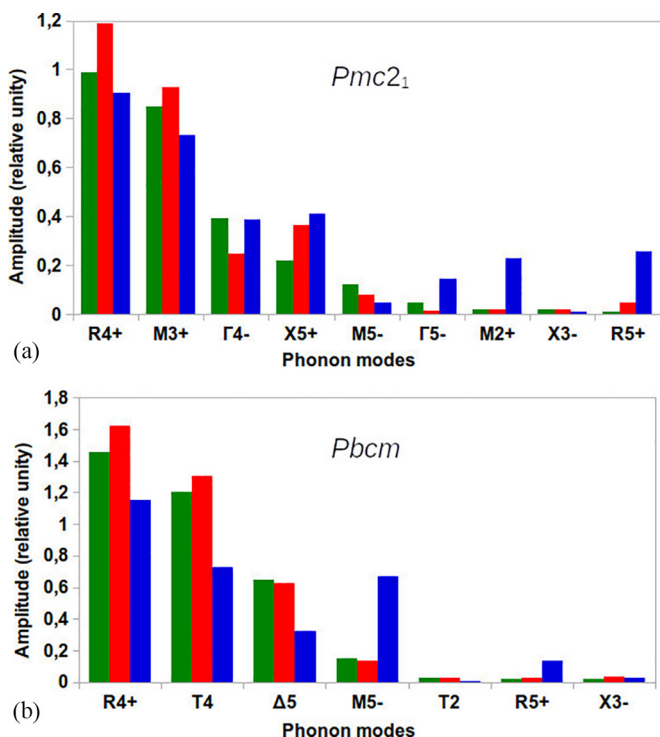


FIG. 4. Relative contributions of phonon modes, analyzed with AMPLIMODES, in the (a)  $Pmc2_1$  and (b)  $Pbcm$  phases of NNO relaxed in GGA-PBESol (green columns) and LDA (red columns) compared to the experimental data (blue columns, Ref. [54]). The main modes consist of either oxygen octahedra rotation ( $R_4^+$ ,  $M_3^+$ , and  $T_4$ ) or polar/antipolar displacements ( $\Gamma_4^-/\Delta_5$ ), while the additional modes consist of couplings with cations ( $M_5^-$ ,  $R_5^+$ ,  $X_3^-$ , and  $X_5^+$ ) or oxygen displacements ( $\Gamma_5^-$ ,  $T_2$ , and  $M_2^+$ ). The  $R3c$  condense to two main modes:  $R_4^+$  (0.89/0.93 [50]) and  $\Gamma_4^-$  (0.42/0.42).

could be formally  $Pca2_1$  rather than  $Pbcm$ , but, in practice, the distortion might not be large enough to be detected and is also likely suppressed at room temperature. The small energy difference between these three structures ( $N$ ,  $P$ ,  $Q$ ), whatever the approximation used, meets the expected criteria for antiferroelectricity [48,53] and is in line with the coexisting ferroelectric and antiferroelectric structures observed in experiments [50].

To go further, let us now analyze the details concerning the three phases that are the subject of our discussion in this section. What are the main and secondary modes that condense in each of these phases and what are their relative contributions? Figure 4 reports the modes that condense in the  $Pmc2_1$  and  $Pbcm$  (some authors use the alternative arrangement  $Pbma$ ) phases.

Concerning the main modes, whatever the approximation used, we notice that, on the one hand, the hierarchy of amplitudes is in agreement with the experimental results, and on the other hand, it is the AFD  $R_4^+$  mode which contributes most to the stabilization of these three phases. However, significant differences from experimental values are observed for some secondary modes that condense in the  $Pbcm$  ( $M_5^-$ ) and  $Pmc2_1$  ( $X_5^+$ ,  $\Gamma_5^-$ ,  $M_2^+$  and  $R_5^+$ ). Given that the  $\Delta_5$  mode, according to our calculations, cannot even condense itself, we can highlight that, in NNO, the AFD  $R_4^+$  mode is very preponderant in the

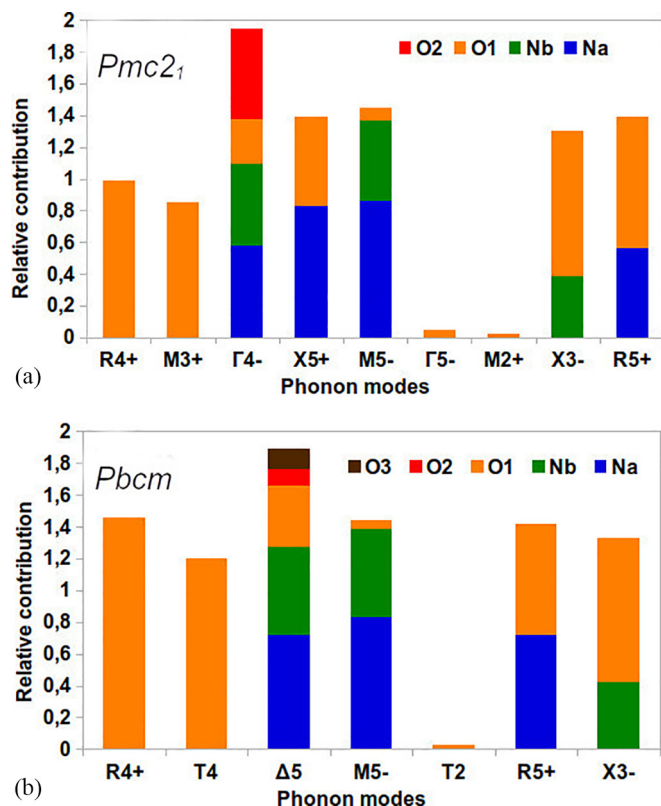


FIG. 5. Atomic contributions by mode in the  $Pmc2_1$  and  $Pbcm$  phases of NNO. The atomic contributions of Na, Nb, and O atoms in the  $\Gamma_4^-$  mode of  $Pmc2_1$  are very close (Na: 0.58; Nb: 0.51; O1:  $-0.57$ ; and O2:  $-0.29$ ), while in the same mode for  $R3c$  it is the Na atom which contributes significantly (Na: 0.72; Nb: 0.32; O1:  $-0.27$ ; and O2:  $-0.55$ ).

coupling with the  $\Delta_5$  mode and thus gives rise to the  $Pbcm$  phase.

It is instructive to compare the relative contribution of each atom to the distortion associated with each irrep (Fig. 5). The colored columns of Fig. 5 allow us to observe that, in NNO, on the one hand, the AFD displacements of the oxygens ( $R_4^+$  and  $M_3^+$ ) are favored over the ferrodistorive displacements ( $\Gamma_5^-$ ,  $M_2^+$ , and  $T_2$ ), on the other hand, the contributions of the atoms are significant and with close intensities in both  $\Gamma_4^-$  polar and  $\Delta_5$ ,  $M_5^-$  antipolar modes. This last observation allows us to argue that the coexistence of low-energy phases is probably related to the simultaneous structural distortion caused by the displacement of Na and Nb ions from their equilibrium positions.

We finally present in Table V how the amplitudes of the modes evolve in the different structures. Interestingly, we can note here that the amplitude of the modes remains the same or increases when they are coupled. This result allows us to argue that the coupling of modes is very favored in NNO to stabilize the phases of the lowest energies. Although they appear as unstable modes in the high-symmetry phase, the  $X_5^-$  ( $103i$ ) and  $M_5^-$  ( $62i$ ) APE modes do not contribute to the stabilization of any of the observed NNO structures. The simultaneous condensation of two (in  $R3c$ ) or three (in  $Pmc2_1$  or  $Pbcm/Pca2_1$ ) of the five main modes as reported in Fig. 4 is sufficient to stabilize them. Comparing the pseudocubic

TABLE V. Evolution of the pseudocubic volume ( $\text{\AA}^3$ ) and amplitudes of the modes in the main structures of NNO.

Symmetry	$V$	$\Gamma_4^-$	$\Delta_5$	$R_4^+$	$T_4$	$M_3^+$
$Pm\bar{3}m$	61.29	$174i$	$129i$	$122i$	$121i$	$120i$
$Amm2$	61.80	0.29				
$P4mbm$	59.26					0.82
$Cmcm$	58.84			0.89		0.92
$Pmmn$	58.80			1.16		1.41
$Pnma$	58.56			1.07		0.82
$Pmc2_1$	59.22	0.39		0.99		0.85
$Pbcm$	59.09		0.65	1.45	1.20	
$R3c$	59.60	0.42		0.89		

volumes of the different structures, we reach the same conclusion as in the PZO [48]; FE and AFE instabilities tend to increase the volume while AFD ones reduce them.

Table VI reports the NNO relaxed positions in the three low-energy structures  $Pmc2_1$ ,  $Pbcm$ , and  $R3c$ , respectively.

TABLE VI. Cell parameters ( $\text{\AA}$ ) and atomic positions of NNO in the orthorhombic  $Pmc2_1$ , orthorhombic  $Pbcm$ , and hexagonal  $R3c$  phases, respectively, in comparison with experimental data.

$Q$	$Pmc2_1$			Ref. [54]		
$a$	7.7421			7.7633		
$b$	5.5024			5.5143		
$c$	5.5608			5.5655		
Site	$x$	$y$	$z$	$x$	$y$	$z$
Na (2a)	0.0000	0.2599	0.0483	0.0000	0.2500	0.7820
Na (2b)	0.5000	0.2588	0.0806	0.5000	0.2510	0.8520
Nb (4c)	0.7495	0.7556	0.0620	0.7500	0.7540	0.8080
O1 (2a)	0.0000	0.6887	0.0377	0.0000	0.1750	0.2630
O2 (2b)	0.5000	0.8132	0.0160	0.5000	0.3220	0.2850
O3 (4c)	0.7175	0.5385	0.3205	0.2300	0.5500	0.0580
O4 (4c)	0.7809	0.0395	0.2462	0.2710	0.9640	0.5130
$P$	$Pbcm$			Ref. [54]		
$a$	5.4945			5.5327		
$b$	5.5602			5.5630		
$c$	15.4732			15.6450		
Site	$x$	$y$	$z$	$x$	$y$	$z$
Na1 (4c)	0.7431	0.2500	0.0000	0.2100	0.7500	0.0000
Na2 (4d)	0.2591	0.7080	0.2500	0.2120	0.7570	0.2500
Nb (8e)	0.2447	0.2270	0.1252	0.2497	0.2500	0.1250
O1 (4c)	0.3139	0.2500	0.0000	0.3260	0.2500	0.0000
O2 (4d)	0.1850	0.2723	0.2500	0.2090	0.2310	0.2500
O3 (8e)	0.4614	-0.0323	0.1418	0.5180	0.0140	0.1370
O4 (8e)	0.0394	0.5419	0.1088	0.9720	0.4670	0.1140
$N$	$R3c$			Ref. [50]		
$a$	5.5241			5.4811		
$b$	5.5241			5.4811		
$c$	13.5313			13.6852		
Site	$x$	$y$	$z$	$x$	$y$	$z$
Na (6a)	0.0000	0.0000	0.5004	0.0000	0.0000	0.2723
Nb (6a)	0.0000	0.0000	0.2592	0.0000	0.0000	0.0164
O (18b)	0.0036	0.5668	0.0238	0.0999	0.3367	0.0833

We can note here again the agreement of our optimized values compared to the previous experimental results.

## VI. SUMMARY

In this work, we conducted a systematic investigation of the energy landscape of  $\text{NaNbO}_3$  through the characterization of various metastable phases, observed and unobserved experimentally. In its high-symmetry cubic perovskite structure, sodium niobate is an insulator with an indirect gap between  $R$  and  $\Gamma$  points of the Brillouin zone. In line with its complex sequence of phase transitions, the phonon dispersion curves of this cubic phase combines distinct polar/antipolar and antiferrodistortive unstable branches. The ground state of  $\text{NaNbO}_3$  does not arise from the condensation of a single unstable mode, but instead from the combination of several modes, which, thanks to their coupling, bring  $\text{NaNbO}_3$  to lower-energy states. Our calculations reveal that, consistently with experimental observations, three phases show very similar lowest energies: rhombohedral FE/AFD  $R3c$  ( $N$  phase),



orthorhombic FE/AFD *Pbcm* (*P* phase), and orthorhombic FE/AFD *Pmc2<sub>1</sub>* (*Q* phase). These three phases mainly arise from the condensation of unstable phonons at *R* and *M* points and along the *T* line connecting them. The GGA-PBEsol functional stabilizes the *R3c* phase as the ground state, consistent with the experiment, and locates the *Pbcm* and *Pmc2<sub>1</sub>* phases together few meV/f.u. above. In contrast, our LDA calculations stabilizes the orthorhombic FE/AFD phase *Pmc2<sub>1</sub>* as the ground state and locates the *Pbcm* phase and then the *R3c* slightly higher in energy, highlighting that LDA should be avoided to study NaNbO<sub>3</sub>. In all calculations we find only small energy differences between the *P*, *N*, and *Q* phases (few meV/f.u.), highlighting the presence of nearly degenerated energy minima fully compatible with antiferroelectricity. The close proximity in the energy and structure of the *Pbcm* and *Pmc2<sub>1</sub>* phases supports the idea that the application of

an electric field could bring the AFE/AFD-*Pbcm* phase to the FE/AFD *Pmc2<sub>1</sub>* phase rather than to the FE/AFD *R3c* phase.

#### ACKNOWLEDGMENTS

This work was supported by the PRD-CCD ARES 2019-2024 project Le coltan du Kivu: Capacité de traitement physico-chimique et études d'applications (Grant No. 32210). Calculations were performed using CECI supercomputer facilities funded by the F.R.S.-FNRS (Grant No. 2.5020.1) and the Tier-1 supercomputer of the Fédération Wallonie-Bruxelles funded by the Walloon Region (Grant No. 1117545) [55].

The authors declare no competing financial interest.

- 
- [1] Z. Liu, T. Lu, J. Ye, G. Wang, X. Dong, R. Withers, and Y. Liu, *Adv. Mater. Technol.* **3**, 1800111 (2018).
- [2] N. Novak, F. Weyland, S. Patel, H. Guo, X. Tan, J. Rödel, and J. Koruza, *Phys. Rev. B* **97**, 094113 (2018).
- [3] M. M. Vopson, G. Caruntu, and X. Tan, *Scr. Mater.* **128**, 61 (2017).
- [4] G. Shirane, R. Newnham, and R. Pepinsky, *Phys. Rev.* **96**, 581 (1954).
- [5] S. Lanfredi, M. H. Lente, and J. A. Eiras, *Appl. Phys. Lett.* **80**, 2731 (2002).
- [6] B. Yang, J. Bian, L. Wang, J. Wang, Y. Du, Z. Wang, C. Wu, and Y. Yang, *Phys. Chem. Chem. Phys.* **21**, 11697 (2019).
- [7] J. H. Jung, M. Lee, J.-I. Hong, Y. Ding, C.-Y. Chen, L.-J. Chou, and Z. L. Wang, *ACS Nano* **5**, 10041 (2011).
- [8] Y. Saito, H. Takao, T. Tani, T. Nonoyama, K. Takatori, T. Homma, T. Nagaya, and M. Nakamura, *Nature (London)* **432**, 84 (2004).
- [9] J.-F. Li, K. Wang, B.-P. Zhang, and L.-M. Zhang, *J. Am. Ceram. Soc.* **89**, 706 (2006).
- [10] A. M. Glazer, *Acta Cryst. B* **28**, 3384 (1972).
- [11] A. M. Glazer, *Acta Cryst. A* **31**, 756 (1975).
- [12] P. M. Woodward, *Acta Cryst. B* **53**, 44 (1997).
- [13] C. Howard and H. Stokes, *Acta Cryst. B* **54**, 782 (1998).
- [14] B. T. Matthias, *Phys. Rev.* **75**, 1771 (1949).
- [15] H. D. Megaw, *Ferroelectrics* **7**, 87 (1974).
- [16] V. A. Shuvaeva, M. Y. Antipin, S. V. Lindeman, O. E. Fesenko, V. G. Smotrakov, and Y. T. Struchkov, *Ferroelectrics* **141**, 307 (1993).
- [17] R. A. Shakhovoy, S. I. Raevskaya, L. A. Shakhovaya, D. V. Suzdalev, I. P. Raevski, Yu. I. Yuzyuk, A. F. Semenchov, and M. El Marssi, *J. Raman Spectrosc.* **43**, 1141 (2012).
- [18] M. D. Peel, S. P. Thompson, A. Daoud-Aladine, S. E. Ashbrook, and P. Lightfoot, *Inorg. Chem.* **51**, 6876 (2012).
- [19] Y. Shiratori, A. Magrez, W. Fischer, C. Pithan, and R. Waser, *J. Phys. Chem. C* **111**, 18493 (2007).
- [20] K. E. Johnston, C. C. Tang, J. E. Parker, K. S. Knight, P. Lightfoot, and S. E. Ashbrook, *J. Am. Chem. Soc.* **132**, 8732 (2010).
- [21] R. Machado, M. Sepliarsky, and M. G. Stachiotti, *Phys. Rev. B* **84**, 134107 (2011).
- [22] Y. Yang, B. Xu, C. Xu, W. Ren, and L. Bellaïche, *Phys. Rev. B* **97**, 174106 (2018).
- [23] X. Gonze, F. Jollet, F. Abreu Araujo, D. Adams, B. Amadon, T. Applencourt, C. Audouze, J.-M. Beuken, J. Bieder, A. Bokhanchuk, E. Bousquet, F. Bruneval, D. Caliste, M. Cote, F. Dahm, F. Da Pieve, M. Delaveau, M. Di Gennaro, B. Dorado, C. Espejo, G. Geneste, L. Genovese, A. Gerossier, M. Giantomassi, Y. Gillet, D. R. Hamann, L. He, G. Jomard, J. Laflamme Janssen, S. Le Roux, A. Levitt, A. Lherbier, F. Liu, I. Lukacevic, A. Martin, C. Martins, M. J. T. Oliveira, S. Ponce, Y. Pouillon, T. Rangel, G.-M. Rignanese, A. H. Romero, B. Rousseau, O. Rubel, A. A. Shukri, M. Stankovski, M. Torrent, M. J. Van Setten, B. Van Troeye, M. J. Verstraete, D. Waroquier, J. Wiktor, B. Xu, A. Zhou, and J. W. Zwanziger, *Comput. Phys. Commun.* **205**, 106 (2016).
- [24] X. Gonze, B. Amadon, G. Antonius, F. Arnardi, L. Baguet, J.-M. Beuken, J. Bieder, F. Bottin, J. Bouchet, E. Bousquet, N. Brouwer, F. Bruneval, G. Brunin, T. Cavignac, J.-B. Charraud, Wei Chen, M. Cote, S. Cottenier, J. Denier, G. Geneste, Ph. Ghosez, M. Giantomassi, Y. Gillet, O. Gingras, D. R. Hamann, G. Hautier, Xu He, N. Helbig, N. Holzwarth, Y. Jia, F. Jollet, W. Lafargue-Dit-Hauret, K. Lejaeghere, M. A. L. Marques, A. Martin, C. Martins, H. P. C. Miranda, F. Naccarato, K. Persson, G. Petretto, V. Planes, Y. Pouillon, S. Prokhorenko, F. Ricci, G.-M. Rignanese, A. H. Romero, M. M. Schmitt, M. Torrent, M. J. van Setten, B. Van Troeye, M. J. Verstraete, G. Zerah, and J. W. Zwanzig, *Comput. Phys. Commun.* **248**, 107042 (2020).
- [25] <http://www.abinit.org>.
- [26] J. P. Perdew, A. Ruzsinszky, G. I. Csonka, O. Vydrov, G. Scuseria, L. Constantin, X. Zhou, and K. Burke, *Phys. Rev. Lett.* **100**, 136406 (2008).
- [27] M. A. L. Marques, M. J. T. Oliveira, and T. Burnus, *Comput. Phys. Commun.* **183**, 2272 (2012).
- [28] D. R. Hamann, *Phys. Rev. B* **88**, 085117 (2013).
- [29] M. J. van Setten, M. Giantomassi, E. Bousquet, M. J. Verstraete, D. R. Hamann, X. Gonze, and G.-M. Rignanese, *Comput. Phys. Commun.* **226**, 39 (2018).

- [30] <http://www.pseudo-dojو.org/index.html>.
- [31] J. P. Perdew and Y. Wang, *Phys. Rev. B* **45**, 13244 (1992).
- [32] X. Gonze and C. Lee, *Phys. Rev. B* **55**, 10355 (1997).
- [33] R. D. King-Smith and D. Vanderbilt, *Phys. Rev. B* **47**, 1651 (1993).
- [34] H. T. Stokes and D. M. Hatch, *J. Appl. Cryst.* **38**, 237 (2005).
- [35] H. T. Stokes, D. M. Hatch, and B. J. Campbell, Isotropy software suite (2007), <https://stokes.byu.edu/iso/isotropy.php>.
- [36] D. Orobengoa, C. Capillas, M. I. Aroyo, and J. M. Perez-Mato, *J. Appl. Cryst.* **42**, 820 (2009).
- [37] B. J. Campbell, H. T. Stokes, D. E. Tanner, and D. M. Hatch, *J. Appl. Cryst.* **39**, 607 (2006).
- [38] H. Kato, H. Kobayashi, and A. Kudo, *J. Phys. Chem. B* **106**, 12441 (2002).
- [39] S. A. Prosandeev, *Phys. Stat. Sol. B* **47**, 2130 (2005).
- [40] R. Oja and R. M. Nieminen, *Phys. Rev. B* **80**, 205420 (2009).
- [41] W. Zhong, R. D. King-Smith, and D. Vanderbilt, *Phys. Rev. Lett.* **72**, 3618 (1994).
- [42] Ph. Ghosez, J.-P. Michenaud, and X. Gonze, *Phys. Rev. B* **58**, 6224 (1998).
- [43] S. E. Ashbrook, L. Le Polles, R. Gautier, C. I. Pickard, and R. I. Walton, *Phys. Chem. Chem. Phys.* **8**, 3423 (2006).
- [44] P. Borlido, J. Schmidt, A. W. Huran, F. Tran, M. A. L. Marques, and S. Botti, *npj Comput. Mater.* **6**, 96 (2020).
- [45] D. I. Bilc, R. Orlando, R. Shaltaf, G.-M. Rignanese, J. Iniguez, and P. Ghosez, *Phys. Rev. B* **77**, 165107 (2008).
- [46] R. I. Eglitis, S. Piskunov, A. I. Popov, J. Purans, D. Bocharov, and R. Jia, *Condens. Matter* **7**, 70 (2022).
- [47] R. I. Eglitis, J. Purans, A. I. Popov, D. Bocharov, A. Chekhovska, and R. Jia, *Symmetry* **14**, 1050 (2022).
- [48] S. Amisi, *Eur. Phys. J. Plus* **136**, 653 (2021).
- [49] C. N. W. Darlington and K. S. Knight, *Acta Cryst. B* **55**, 24 (1999).
- [50] S. K. Mishra, N. Choudhury, S. L. Chaplot, P. S. R. Krishna, and R. Mittal, *Phys. Rev. B* **76**, 024110 (2007).
- [51] H. Shimizu, H. Guo, S. E. Reyes-Lillo, Y. Mizuno, K. M. Rabe, and C. A. Randall, *Dalton Trans.* **44**, 10763 (2015).
- [52] C. N. W. Darlington and H. D. Megaw, *Acta Cryst. B* **29**, 2171 (1973).
- [53] K. M. Rabe, *Antiferroelectricity in Oxides: A Reexamination, Functional Metal Oxides: New Science and Novel Applications*, edited by S. Ogale and V. Venkateshan (Wiley, New York, 2012).
- [54] J. Koruza, J. Tellier, B. Malič, V. Bobnar, and M. Kosec, *J. Appl. Phys.* **108**, 113509 (2010).
- [55] [https://www.ulg.ac.be/cms/c\\_3826073/fr/nic4](https://www.ulg.ac.be/cms/c_3826073/fr/nic4), <http://www.ceci-hpc.be/>.